

## Article

# Rhodium-Based Catalysts: An Impact of the Support Nature on the Catalytic Cyclohexane Ring Opening

Kristina E. Kartavova<sup>1,2</sup>, Mikhail Yu. Mashkin<sup>1,2,3</sup> , Mikhail Yu. Kostin<sup>1</sup>, Elena D. Finashina<sup>3</sup>,  
Konstantin B. Kalmykov<sup>1</sup>, Gennady I. Kapustin<sup>3</sup>, Petr V. Pribytkov<sup>1,3</sup>, Olga P. Tkachenko<sup>3</sup> , Igor V. Mishin<sup>3</sup>,  
Leonid M. Kustov<sup>1,2,3,\*</sup> and Alexander L. Kustov<sup>1,2,3</sup>

<sup>1</sup> Department of Chemistry, Lomonosov Moscow State University, 119991 Moscow, Russia

<sup>2</sup> Institute of Ecotechnologies, National University of Science and Technology "MISiS", 119049 Moscow, Russia

<sup>3</sup> N.D. Zelinsky Institute of Organic Chemistry RAS, 119991 Moscow, Russia

\* Correspondence: lmkustov@mail.ru

**Abstract:** Because of the growing demand for high-quality fuels, the light cycle oil fraction improvement including cetane number improvement is important. The main way to reach this improvement is the ring opening of cyclic hydrocarbons, and a highly effective catalyst should be found. Cyclohexane ring openings are a possible option to investigate the catalyst activity. In this work, we investigated rhodium-loaded catalysts prepared using the commercially available industrial supports: single-component ones, SiO<sub>2</sub> and Al<sub>2</sub>O<sub>3</sub>; and mixed oxides CaO + MgO + Al<sub>2</sub>O<sub>3</sub> and Na<sub>2</sub>O + SiO<sub>2</sub> + Al<sub>2</sub>O<sub>3</sub>. The catalysts were prepared by incipient wetness impregnation and investigated by N<sub>2</sub> low-temperature adsorption-desorption, XRD, XPS, DRS UV-Vis and DRIFT spectroscopy, SEM, and TEM with EDX. The catalytic tests were performed in cyclohexane ring opening in the range of 275–325 °C. The best result was demonstrated by the sample 1Rh/CaMgAlO: the selectivity to *n*-hexane was about 75% while the cyclohexane conversion was about 25% at 275 °C. The space-time yield was up to 12 mmol<sub>*n*-hexane</sub> g<sub>cat</sub><sup>-1</sup>h<sup>-1</sup>.

**Keywords:** rhodium; support; cyclohexane; ring opening; heterogeneous catalysis; gas phase reaction; cetane number; fuel upgrading



**Citation:** Kartavova, K.E.; Mashkin, M.Y.; Kostin, M.Y.; Finashina, E.D.; Kalmykov, K.B.; Kapustin, G.I.; Pribytkov, P.V.; Tkachenko, O.P.; Mishin, I.V.; Kustov, L.M.; et al. Rhodium-Based Catalysts: An Impact of the Support Nature on the Catalytic Cyclohexane Ring Opening. *Nanomaterials* **2023**, *13*, 936. <https://doi.org/10.3390/nano13050936>

Academic Editor: Detlef W. Bahnemann

Received: 1 February 2023

Revised: 23 February 2023

Accepted: 1 March 2023

Published: 4 March 2023



**Copyright:** © 2023 by the authors. Licensee MDPI, Basel, Switzerland. This article is an open access article distributed under the terms and conditions of the Creative Commons Attribution (CC BY) license (<https://creativecommons.org/licenses/by/4.0/>).

## 1. Introduction

High-quality fuels nowadays are highly demanded and the demand is steadily and significantly increasing. There is an option to blend the diesel fuel with the light cycle oil (LCO) fraction. Such an option is possible because the composition of this fraction is appropriate in terms of the number of carbon atoms. However, there is a problem to meet the standards of diesel fuel in the cetane number (the desired cetane number is  $\geq 47$ ) and the polyaromatics content. Hydrogenation of polyaromatics can partially solve the problem and decrease the content of polyaromatics, but the production of naphthenic substances does not solve the problem of the cetane number, so the ring-opening process should be applied [1]. The comparison of the cetane number of different hydrocarbons demonstrates that the linear alkanes are the most preferable ones, and much less preferable but still appropriate are the monobranched alkanes. At the same time, the length of the carbon chain plays a significant role: the longer the chain, the higher the cetane number [2,3]. That is why the highly active and selective linear alkanes catalysts of the ring-opening reaction should be found to improve the cetane number of the diesel produced from LCO.

In order to investigate the process of ring opening, different cyclic hydrocarbons are used: mostly decalin, but also tetralin, perhydroindane, methylcyclohexane, etc. [4]. As a model reaction of ring opening, cyclohexane opening can be applied [5–7], because the cyclohexane molecule is the simplest cyclic hydrocarbon with good stability. Sometimes other cyclic hydrocarbons are used [4].

The catalysts applied in the ring opening reaction can be monofunctional acidic catalysts or metal catalysts deposited on the acidic or non-acidic supports to form bifunctional or monofunctional metallic catalysts, respectively [8]. By using decalin transformations, the following mechanisms were proposed: the mechanism through carbocation formation on the monofunctional acid catalysts promoting the isomerisation; hydrogenolysis/hydrocracking mechanism over the monofunctional metallic catalysts leading to a higher ring opening selectivity and lower selectivity to branched products but in this case, the conversions of decalin are low; and the bifunctional ring-opening mechanism, which seems to be the optimal one for LCO improvement because of the rather high activity and selectivity to ring-opening products and lower selectivity to branching and hydrocracking [9].

Despite the attempts to use non-noble metal catalysts, such as W-based [1] or Ni-Mo-based [10], the most active and selective catalysts are so far the catalysts based on noble metals. From the reported supported noble metal catalysts based on Rh, Ru, and Pt, the most active and selective to linear alkanes were the Rh-based ones [7]. Ir-based catalysts are sometimes applied, they also demonstrate rather good performance in the ring opening [4,11]. Bimetallic catalysts are reported to be rather active and selective, but the comparison of them with monometallic systems not always demonstrates significant improvement: nevertheless, in some cases, the yields to the products of the ring-opening reaction are higher than for monometallic catalysts [12]. The time dependence of the catalytic performance was evaluated for the bimetallic Pt-Ir catalysts with different compositions, and it was shown that the product yield distribution changed in time: with increasing time on stream, carbon deposition occurs, while the ring contraction processes are suppressed and the ring opening conversion increases [13]. Nevertheless, Rh as an active metal is widely used and also it seems to be rather promising in the reaction of cyclohexane ring opening, so the investigation of the systems based on this metal are to be conducted.

The monometallic catalysts  $x\text{Rh}/\text{SiO}_2\text{-Al}_2\text{O}_3$  with different Rh loadings were investigated in the decalin ring opening and it was revealed that there was an optimal Rh content for the ring opening and suppression of any other processes, in this case, it was 1.5 wt% [14]. The thermodynamic analysis shows that the optimal temperature for a decalin ring opening is about 225 °C [15]. At the same time, an increase in the hydrogen/hydrocarbon ratio leads to increasing thermodynamic yields of the ring opening process and to decreasing dehydrogenation product yields [15].

A large number of studies are devoted to the estimation of the support nature impact on the catalytic activity: the traditional supports are usually applied such as zeolitic materials or porous alumina, silica, or titania [16–18]. An example of the successful application of SBA-15 silicate has been reported [19]. It is proven that both the acidic sites of the support and the metal sites play a certain role in the process [20]. It has been reported that the acidic sites of a medium strength favour the process of ring opening along with isomerisation and cracking, but the cracking process plays a significant role in the case when strong acid sites are present in the zeolite [21]. The influence of residual chlorine is investigated for Pt, Rh, and Ir catalysts, and it is revealed that the behaviour of the catalyst depends on the metal and support nature. Particularly, the Rh catalysts demonstrate both the direct cyclic hydrocarbon conversion and the bifunctional mechanism with the participation of the acidic sites of the chlorinated support [22]. The attempts to create a single catalyst that is capable of providing aromatics hydrogenation and the following ring opening reaction are described, for example [23,24].

This work is aimed at the preparation of Rh catalysts on the commercial supports: silica and alumina-based, their physicochemical characterisation and catalytic tests in the reaction of selective cyclohexane ring opening to explore the influence of the support on the catalytic activity and selectivity to certain products.

## 2. Materials and Methods

### 2.1. Materials

In this work, we used the following reagents: the supports SiO<sub>2</sub> (CAS 7631-86-9), Al<sub>2</sub>O<sub>3</sub> (CAS 1344-28-1), the mixture of CaO + MgO + Al<sub>2</sub>O<sub>3</sub> (CAS 1305-78-8, 1309-48-4, 1344-28-1), the mixture of Na<sub>2</sub>O + SiO<sub>2</sub> + Al<sub>2</sub>O<sub>3</sub>. All the supports were purchased from Saint Gobain (Courbevoie, France) and were fractioned to obtain the particles with a size of 0.25–0.5 mm. (NH<sub>4</sub>)<sub>3</sub>RhCl<sub>6</sub>·xH<sub>2</sub>O ( $x \approx 1$ ) from Alfa Aesar (Ward Hill, MA, USA) and distilled water were used for the catalyst preparation.

### 2.2. Methods

Textural analysis of the supports was performed by measuring N<sub>2</sub> adsorption-desorption isotherms at 77 K using an ASAP 2020 Plus unit (Micromeritics, Norcross, GA, USA). The BET, BJH, and *t*-plot techniques were used to derive the specific surface area and porosity from the adsorption-desorption isotherms. The micropore size distribution was derived from the DFT model of cylindrical pores for an oxide surface. Before N<sub>2</sub> adsorption, the samples were evacuated at 300 °C at 10<sup>−5</sup> Torr for 4 h.

SEM images and EDX data were collected using an electron microscope LEO EVO 50 XVP (Karl Zeiss, Oberkochen, Germany) with an energy-dispersive spectrometer INCA—Energy 350 (Oxford Instruments, Abingdon, UK).

Transmission electron microscopy studies were performed using an aberration-corrected JEOL JEM-2100F/Cs (JEOL Ltd., Tokyo, Japan) equipped with EDX.

The XPS spectroscopic characterisation was performed with an X-ray photoelectron spectrometer PHI5000 Versa Probe II with the source of excitation—monochromatized Al K $\alpha$  radiation (1486.6 eV, 50 W). The spot of analysis was 200  $\mu$ m. The powders made from the catalysts were pressed into an In foil to make a continuous layer. Element analyses were performed by the method of the relative element sensitivity factors using integral intensities of the following lines: O 1s, Si 2s, Al 2p, Rh 3d. High-resolution spectra were collected at the transmission energy of 23.5 eV. The density of the data collection was 0.2 eV per step. Binding energies were derived from the high-resolution spectra. The binding energy scale was calibrated by the lines of Au 4f<sub>7/2</sub>—83.96 eV, and Cu 2p<sub>3/2</sub>—932.62 eV.

UV-Vis diffuse reflectance spectra were collected using a spectrophotometer Shimadzu UV-3600 Plus (Shimadzu Corp., Kyoto, Japan) equipped with an integrating sphere ISR-603 at room temperature. The range of wavelengths was 300–700 nm. Barium sulphate was used as a diluent.

DRIFT spectra were collected using a spectrometer NICOLET Protege 460 equipped with a diffuse reflectance console engineered at the Zelinsky Institute of Organic Chemistry [25] at room temperature. The range of the wavenumbers was 6000–400 cm<sup>−1</sup> with a 4 cm<sup>−1</sup> step. The number of the collected spectra was 500 to obtain the appropriate signal-to-noise ratio. Before the spectra collection, the samples were heated at 400 °C under the pressure of 10<sup>−3</sup> Torr for 2 h, the rate of heating was 5 °C per minute. CD<sub>3</sub>CN was chosen as a test molecule. Adsorption of CD<sub>3</sub>CN was conducted at room temperature and saturated vapour pressure of 96 Torr. Intensities of the absorbance bands were derived in Kubelka-Munk (KM) units. A powder of CaF<sub>2</sub> was used as a standard. Spectra collection and processing were performed with the OMNIC software (ThermoFischer Scientific Corp., Waltham, MA, USA). The spectra were presented as a difference between the spectra before and after adsorption.

TPR-H<sub>2</sub> studies were carried out in a half-automatized flow system with a water trap cooled down to −100 °C. The detector (TCD) was calibrated by reduction of CuO (Aldrich-Chemie GmbH, Burlington, MA, USA, 99%). Prior to the measurements, the samples were pretreated in an Ar flow with a gas flow rate of 30 mL min<sup>−1</sup> at 300 °C. Then the catalysts were heated to 850 °C at the rate of 10 °C/min in a 5% H<sub>2</sub>–Ar gas mixture.

X-ray diffraction analysis was performed after the calcination of the samples using an ARL X'TRA diffractometer (ThermoFischer Scientific Corp., Waltham, MA, USA) with

CuK $\alpha$  radiation (40 kV, 40 mA) with a scanning rate of 1.2° per minute over the scanning range of  $10 < 2\theta < 70^\circ$ . ICCD data were used for identification purposes.

The catalytic reaction of cyclohexane ring opening was performed at temperatures in the range of 275–325 °C, the pressure was 40 atm, the feed mixture consisted of 0.0170 mL of liquid cyclohexane further vaporized per min, and H<sub>2(g)</sub> (50 mL per min). Therefore, the molar ratio H<sub>2</sub>/C<sub>6</sub>H<sub>12</sub> was 14. The analysis of the reaction products was conducted with a gas chromatograph Chromatec Crystal 5000.2 equipped with two thermal conductivity detectors and two flame ionisation detectors, and capillary columns Hayesep 1 m × 2 mm, NaX 3 m × 2 mm, Hayesep 3 m × 2 mm, GasPro 60 m × 0.32 mm, and ZB-1 60 m × 0.32 mm. The data were processed with the software package Chromatec Analytic 3 (Chromatec Ltd., Ioshkar-Ola, Russia). The catalyst loading was 0.3 cm<sup>3</sup>, the masses were 100–150 mg, and the size of the particles was in the range of 0.25–0.5 mm.

The selectivity to *n*-hexane (*s*) and space-time yield (STY) of *n*-hexane were calculated by the following formulae:

$$s = \frac{n_{C_6H_{14}}}{n_{C_6H_{14}} + \sum n_i'}$$

where  $n_i$  is the number of moles of each product of the reaction excluding *n*-hexane.

$$STY = \frac{X_{C_6H_{12}} s n_{cyclohexane}^{inlet}}{m_{catalyst}}$$

where  $X(C_6H_{12})$  is the cyclohexane conversion, *s* is the selectivity to *n*-hexane,  $n_{cyclohexane}^{inlet}$  is the inlet flow of cyclohexane (mmol h<sup>−1</sup>), and  $m_{catalyst}$  is the mass of the catalyst (g).

### 2.3. Synthetic Procedure

The syntheses were performed by the wet impregnation method of the commercial supports: SiO<sub>2</sub>, Al<sub>2</sub>O<sub>3</sub>, the mixture of CaO + MgO + Al<sub>2</sub>O<sub>3</sub>, and the mixture of Na<sub>2</sub>O + SiO<sub>2</sub> + Al<sub>2</sub>O<sub>3</sub>. The supports were impregnated with a solution prepared from (NH<sub>4</sub>)<sub>3</sub>RhCl<sub>6</sub>·H<sub>2</sub>O to obtain the catalyst with the following composition:  $m_{Rh}/(m_{Rh} + m_{support}) = 0.01$ . The impregnated samples were dried at 60–90 °C for 2 h and calcined at 550 °C for 4 h. The temperature of the calcination and the reduction were chosen on the basis of TG and TPR-H<sub>2</sub> analysis of a model sample presented in Supplementary Materials (Figure S1). The obtained catalysts were denoted as 1Rh/SiO<sub>2</sub>, 1Rh/Al<sub>2</sub>O<sub>3</sub>, 1Rh/CaMgAlO, 1Rh/NaSiAlO. Rhodium(III) oxide was reduced with H<sub>2</sub> before the catalytic tests at the fixed-bed flow-type stainless steel reactor under an H<sub>2</sub> flow of 50 mL per min at 450 °C ( $p_{H_2} = 40$  atm) for 3 h.

## 3. Results

### 3.1. BJH–BET Measurements

The supports were examined by the low-temperature N<sub>2</sub> adsorption-desorption method (Figure 1, Table 1). All the samples are mostly mesoporous, with a small volume of micropores. The surface areas are rather large, and except for Al<sub>2</sub>O<sub>3</sub>, the surface areas are larger than 200 m<sup>2</sup>g<sup>−1</sup>. The mesopore size distribution maxima are different, and they increase in the following sequence: NaSiAlO < CaMgAlO < Al<sub>2</sub>O<sub>3</sub> < SiO<sub>2</sub>. The total pore volume of the samples also differs, and the most porous sample is SiO<sub>2</sub>, whereas the least porous material is Al<sub>2</sub>O<sub>3</sub>. Pore size distributions of the mixed supports are similar to each other. The DFT model calculations revealed pore size distributions in the region of micropores. Noticeably, the mixed supports CaMgAlO and NaSiAlO have almost the same PSD in the region of micropores, but the sample NaSiAlO has an additional PSD peak at the border between micro- and mesopores. Since the peak is located in the region of small mesopores, it affects the surface area significantly. That is why the surface area of the sample NaSiAlO is the largest.

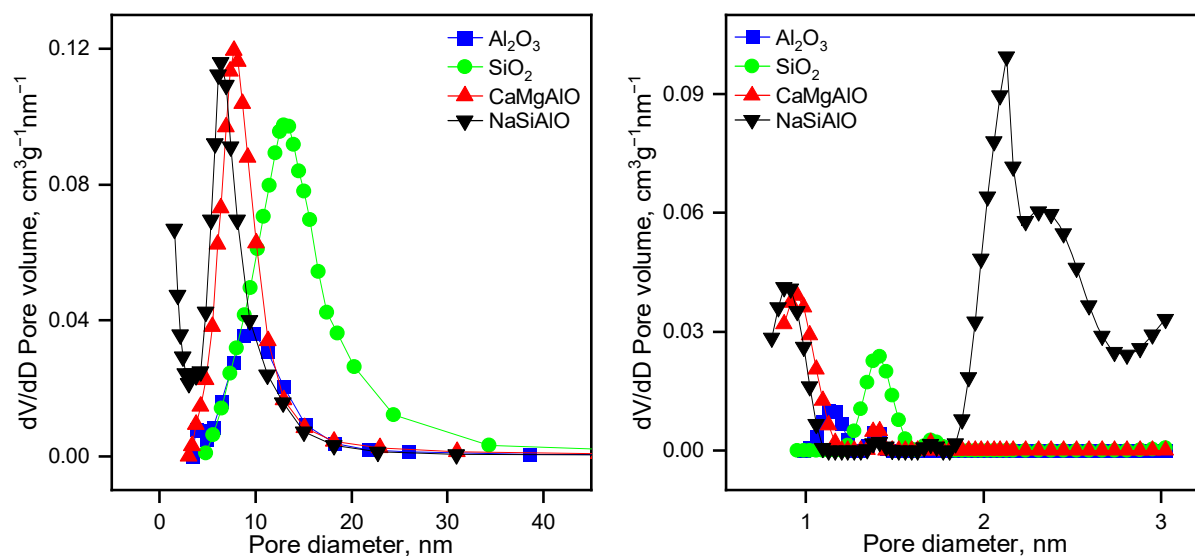


**Figure 1.** Meso- (left) and micro- (right) pore size distributions for the samples of the supports.

**Table 1.** The textural properties of the supports of the catalysts derived by the N<sub>2</sub> low-temperature adsorption-desorption technique.

Sample	S <sub>BET</sub> , m <sup>2</sup> g <sup>-1</sup>	V <sub>total</sub> , cm <sup>3</sup> g <sup>-1</sup>	V <sub>meso</sub> , cm <sup>3</sup> g <sup>-1</sup>	V <sub>micro</sub> , cm <sup>3</sup> g <sup>-1</sup>	D <sub>max</sub> , nm
SiO <sub>2</sub>	239	0.92	0.92	0.005	12.9
Al <sub>2</sub> O <sub>3</sub>	96	0.27	0.27	0.016	9.8
CaMgAlO	245	0.58	0.57	0.011	7.7
NaSiAlO	410	0.58	0.57	0.015	1.6, 6.4

The isotherms of nitrogen adsorption-desorption are presented in Supplementary Materials (Figure S2). All the isotherms are of type IV according to the IUPAC classification [26].

### 3.2. XRD

The samples of the supports were investigated by XRD. The SiO<sub>2</sub> sample demonstrates only a wide halo in the range of 10–30 degrees (Figure 2). It should be assigned to amorphous silica. The intensity of such a halo in the case of the SiO<sub>2</sub> sample is larger than that in the case of NaSiAlO, seemingly such behaviour should be attributed to a different silica phase content in the sample. The mixed support NaSiAlO demonstrates a wider halo at 10–30 degrees and additional weak wide reflexes of Al<sub>2</sub>O<sub>3</sub>. The diffractograms of the supports Al<sub>2</sub>O<sub>3</sub> and CaMgAlO demonstrate only the reflexes referred to as the -Al<sub>2</sub>O<sub>3</sub> phase. Noticeably, the intensity of the reflexes corresponding to Al<sub>2</sub>O<sub>3</sub> decreases in the following order: Al<sub>2</sub>O<sub>3</sub> > CaMgAlO > NaSiAlO. This can be caused by a decrease in the Al<sub>2</sub>O<sub>3</sub> phase amount.

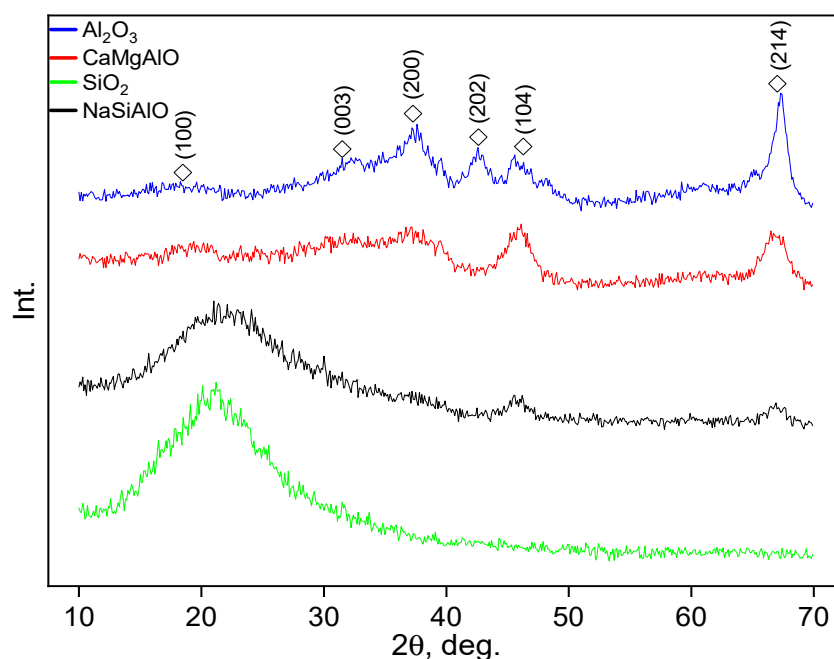


**Figure 2.** Diffractograms of the supports. The figure contains the reference reflexes of the phase  $\gamma$ - $\text{Al}_2\text{O}_3$  shown as M: the ICDD card number [00-013-0373].

### 3.3. SEM and EDX Characterisation

The SEM examination of the prepared catalysts revealed the difference in the rhodium distribution on the surfaces (Figure 3). In the case of the catalysts with single-component supports, 1Rh/ $\text{SiO}_2$  and 1Rh/ $\text{Al}_2\text{O}_3$ , deposited rhodium are distributed evenly on the surfaces. The black side areas on the Rh maps and microphotos can be attributed to the areas out of the support particles.

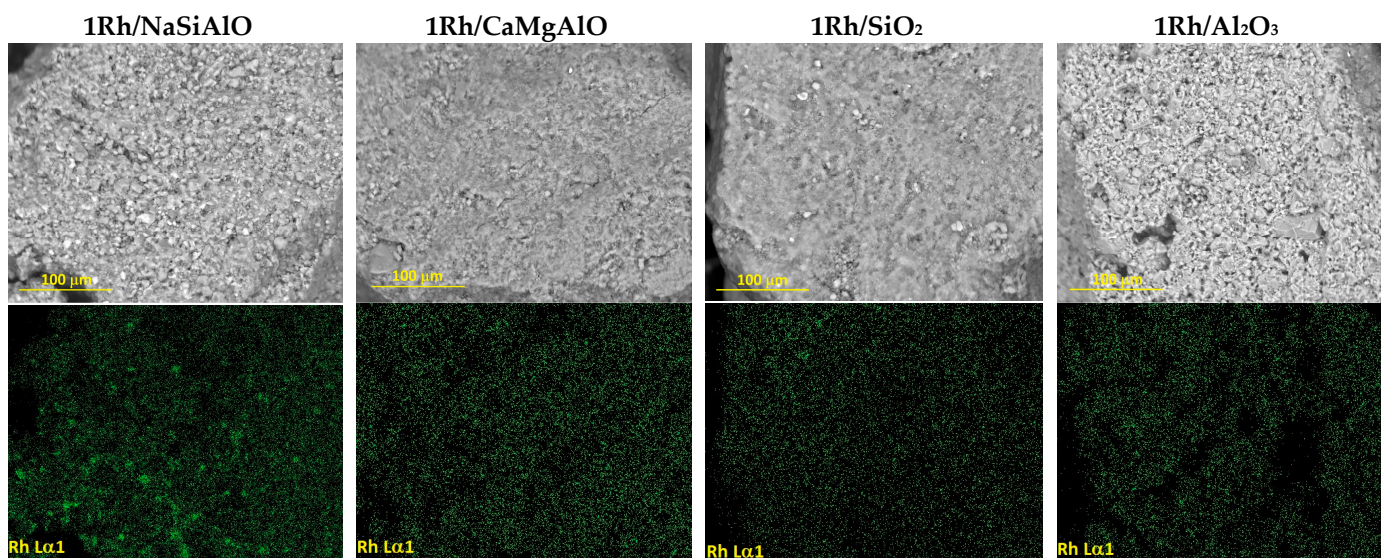


**Figure 3.** SEM images (the upper row) and rhodium distribution maps (the lower row) of the rhodium-containing catalysts.

The catalysts with mixed supports, 1Rh/NaSiAlO and 1Rh/CaMgAlO, demonstrate a difference in the rhodium distribution: the sample 1Rh/NaSiAlO has inhomogeneous rhodium distribution, i.e., the areas with higher Rh atoms concentrations on the catalyst surface can be seen as light spots on the picture, and the regions with a small Rh atoms concentration can be found as dark ones. It means that the areas of higher and lower Rh concentrations can be seen on the map.

So, all the samples, excluding 1Rh/NaSiAlO, have evenly distributed Rh on their surfaces, but the sample 1Rh/NaSiAlO has an inhomogeneous rhodium distribution.

Additional SEM images and the results of EDX can be found in Supplementary Materials, Table S1.

### 3.4. TEM

All the prepared catalysts were examined by TEM (Figure 4). TEM investigation of the rhodium-loaded catalysts revealed the difference in the particle size distribution. 1Rh/Al<sub>2</sub>O<sub>3</sub> contains observable particles with a size of about 20 nm, CaMgAlO—18–23 nm, NaSiAlO—13–19 nm, and SiO<sub>2</sub>—2–8 nm. So, the smallest particles are present in the SiO<sub>2</sub>-supported catalyst, and the largest—in the CaMgAlO-based catalyst. Rhodium is present not in all the EDX spectra for each sample. It may indicate that Rh atoms do not cover all of the surfaces, but it is distributed in a form of relatively small particles. EDX spectra for the samples can be found in Supplementary Materials (Figures S3 and S4).

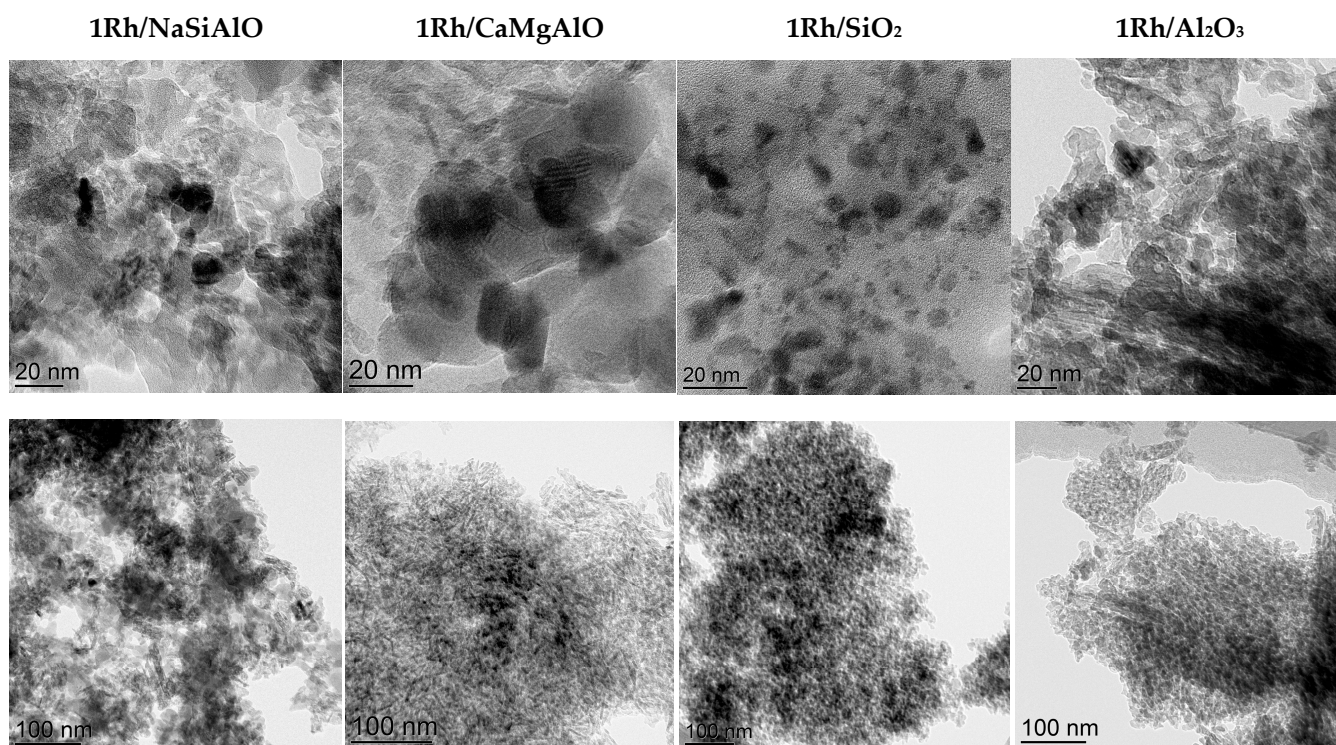


**Figure 4.** TEM images of the initially calcined in air catalysts with different supports.

The measured interplanar spacings for the sample 1Rh/SiO<sub>2</sub> were 0.36, and 0.33 nm for the areas of crystallinity on the TEM picture (Figure 5). These interplanar spacings correspond to a Rh<sub>2</sub>O<sub>3</sub> phase, the ICDD card number [24-924]. The revealed interplanar spacings for the sample 1Rh/NaSiAlO were 0.36, 0.22, and 0.23 nm for the different areas on the TEM image. These interplanar distances also correspond to the Rh<sub>2</sub>O<sub>3</sub> phase. The estimation of the phase composition was performed because of the impossibility to determine it from XRD data.

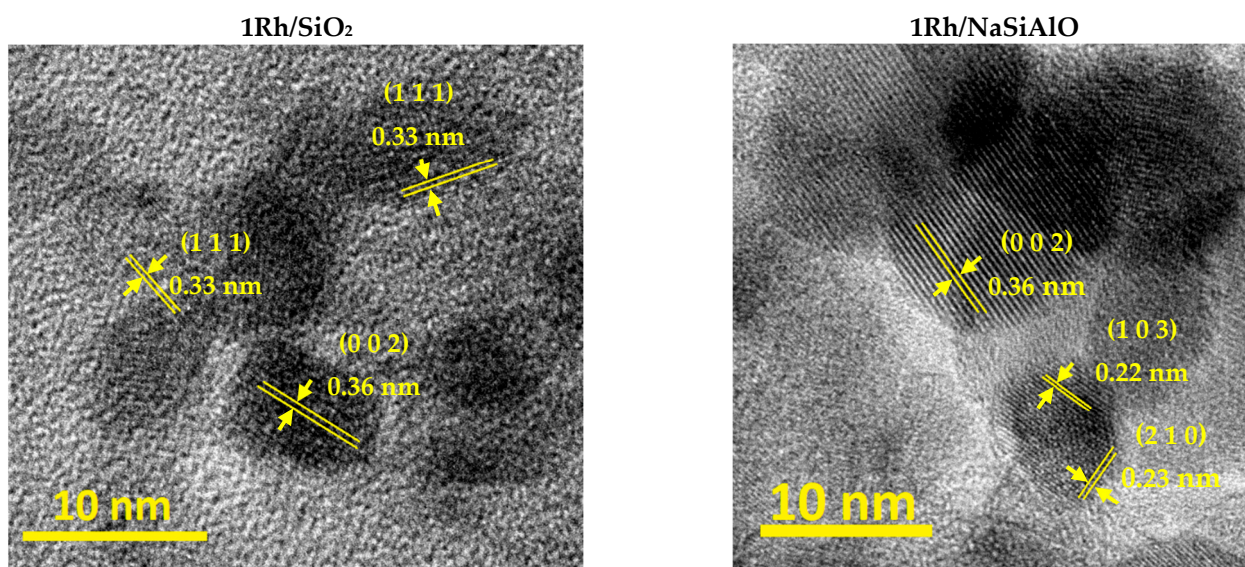


**Figure 5.** TEM images of the initially calcined in air catalysts with Si-containing supports. The crystal planes are indicated in the pictures.

The two other catalysts (prepared from the supports without silica) do not demonstrate any crystal planes. Perhaps, it results from the support nature and the specificity of the support-metal sites interaction in terms of the effect of Bronsted acidity. Nevertheless, the catalysts were used only after reduction in an H<sub>2</sub> flow, which is why the rhodium (III) oxide phase is transformed into the metal state.

The catalysts with silicon-containing supports were additionally investigated after reduction with H<sub>2</sub> (Figure 6). It can be seen that the samples contain small Rh-containing particles (dark points in the pictures).

The distribution of Rh particles by size (Figure 7) differs from the sample 1Rh/SiO<sub>2</sub> initially calcined in air to a reduced one. It can be seen that the distribution became bimodal, a maximum at 4 nm disappeared and two smaller maxima appear at 2 and 5 nm (seemingly because of reduction). Moreover, in the case of the sample 1Rh/NaSiAlO, it became possible to reveal the rhodium nanoparticles on the surface only after the reduction. Figure 8 provides TEM images of the reduced samples 1Rh/CaMgAlO and 1Rh/Al<sub>2</sub>O<sub>3</sub>. It can be noticed that, after the reduction, the nanoparticles of Rh appeared, but the numbers of observable particles for these samples are less than for the samples with silica-based supports. Generally, it can be seen that all the samples being reduced demonstrate the nanoparticles of Rh, while only silica-based ones do in the case of calcined in air samples.

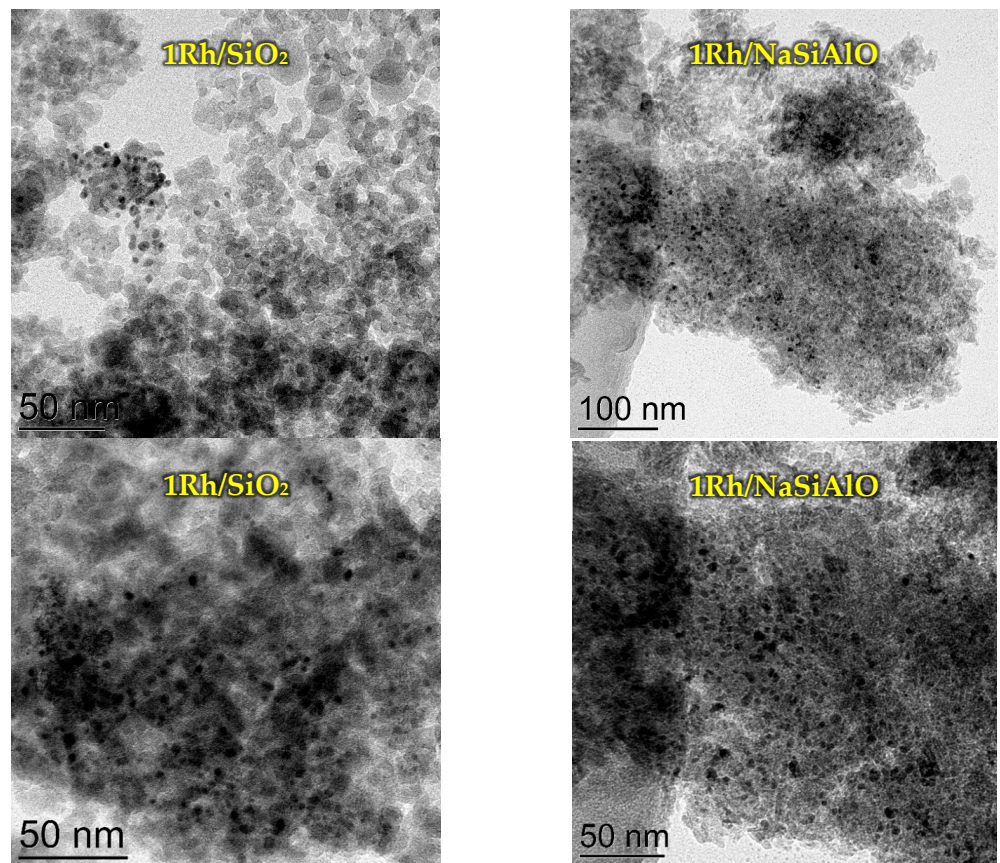


Figure 6. TEM images of the reduced H<sub>2</sub> catalysts with Si-containing supports.

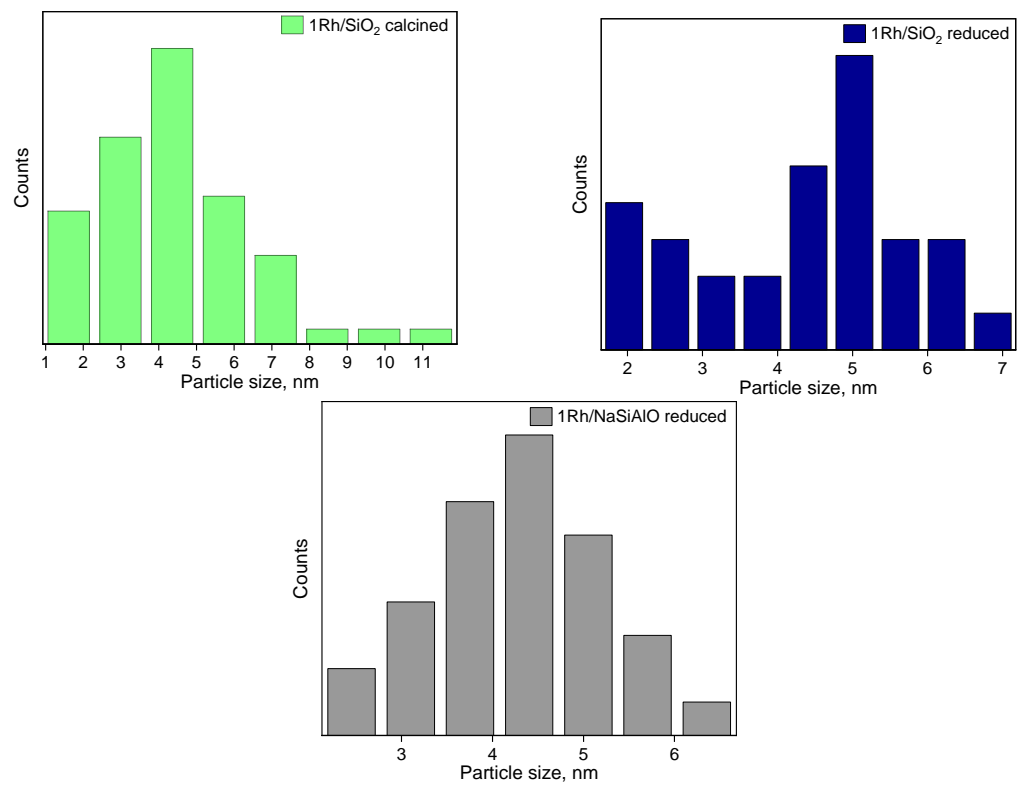
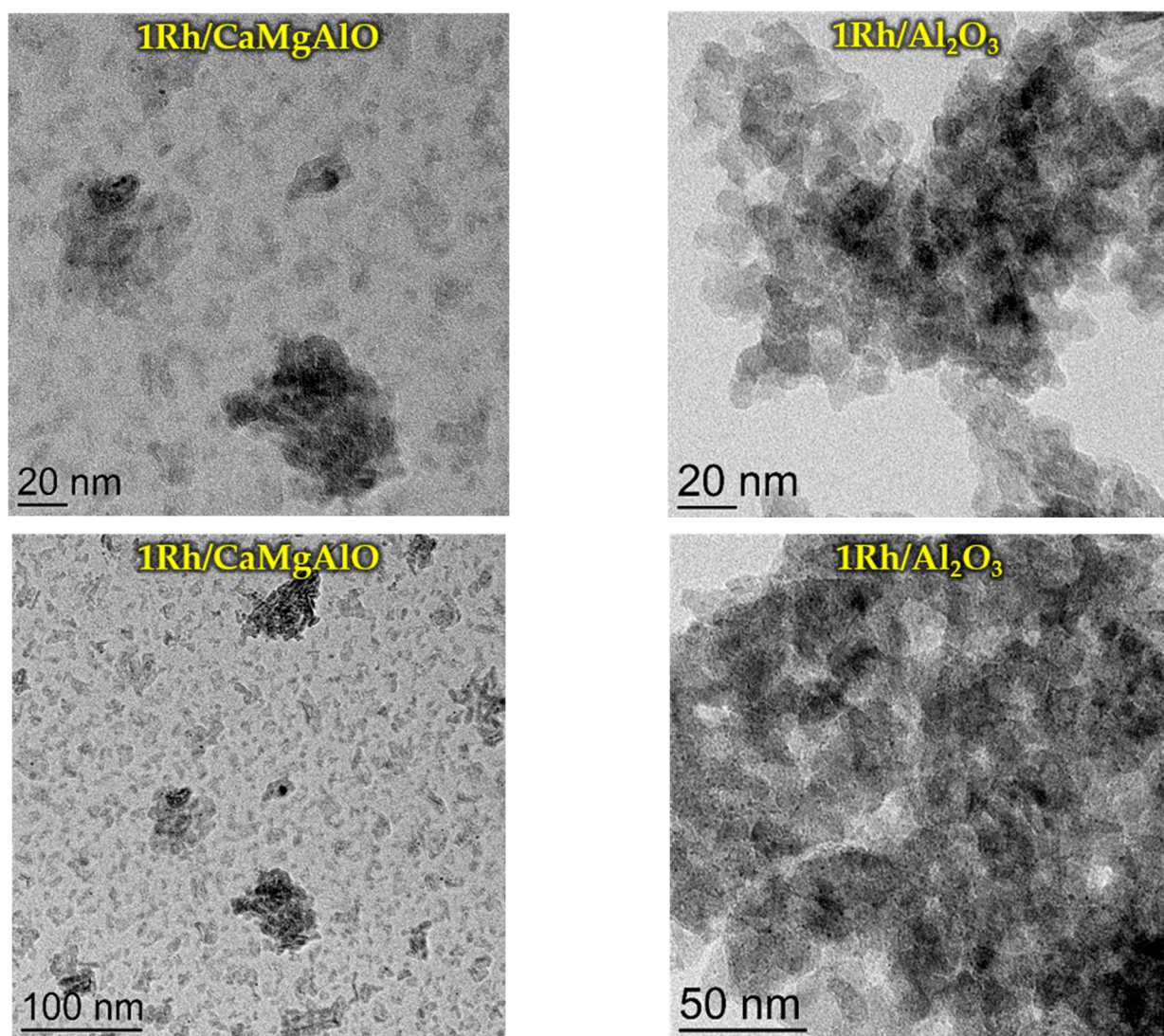


Figure 7. Rh particle distribution by size in the case of initially calcined in air and reduced catalysts.



**Figure 8.** TEM images of the reduced  $H_2$  catalysts with Al-containing supports.

### 3.5. UV-Vis Diffuse Reflectance Spectroscopy

The UV-Vis DRS results can be found in Supplementary Materials (Figure S5) with the interpretation of  $Rh^{3+}$  bands [27–29].

### 3.6. DRIFT Spectroscopy

All the supports used for the catalyst preparation were investigated by DRIFT spectroscopy.

The results for the single-component supports, i.e.,  $Al_2O_3$  and  $SiO_2$ , are presented in Figure 9, Tables 2 and 3. In the case of  $Al_2O_3$ , it can be seen that the intensity of each of the four observed bands is higher for the sample after the adsorption of  $CD_3CN$  compared to the sample after evacuation under heating. In the case of  $SiO_2$ , the intensity of the band in the spectrum of the evacuated sample decreased while a new wideband appeared. The assignment of all the bands is given in Tables 2 and 3. The difference in the spectra before and after  $CD_3CN$  adsorption gives the values of the shifts of  $201\text{ cm}^{-1}$  and  $298\text{ cm}^{-1}$ , respectively. It indicates that the sample of  $Al_2O_3$  contains weak Brønsted acid sites (BAS) on the surface, while  $SiO_2$  contains moderate ones. Both these observations are proven by the shifts of the CN stretching vibration band. The alumina support also contains Lewis acid sites (LAS) on the surface (Table 3). The  $Al_2O_3$  support demonstrates a disappearance of the band from BAS, while LAS bands are present in the spectrum up to  $100\text{ }^\circ\text{C}$  under evacuation. At the same time, the band from BAS disappears in the spectrum of  $SiO_2$

already at room temperature during evacuation. The band in the region of 2110–2120  $\text{cm}^{-1}$  corresponds to the bending vibrations of  $\text{CD}_3$  groups.

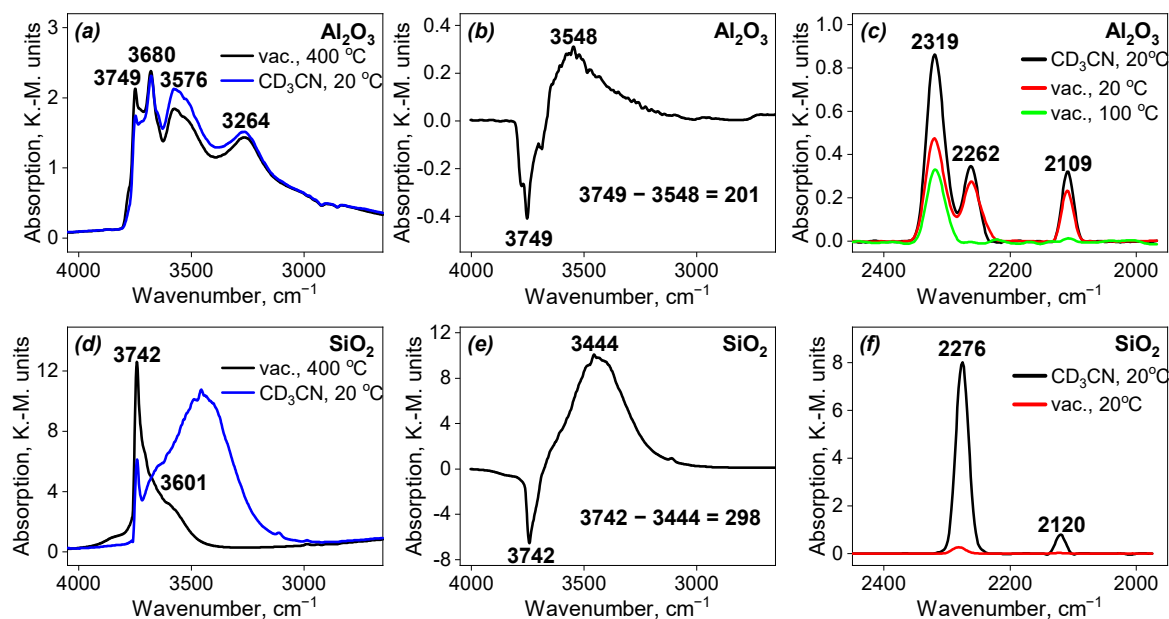


**Figure 9.** Spectra of single-component supports: (a,d) DRIFT-OH after evacuation and after adsorption of  $\text{CD}_3\text{CN}$ ; (b,e) difference of the DRIFT-OH spectra before and after adsorption of  $\text{CD}_3\text{CN}$ ; (c,f) DRIFT- $\text{CD}_3\text{CN}$  adsorption-desorption spectra of the support.

**Table 2.** The assignment of DRIFT spectroscopy bands in the region of OH groups.

Sample	Frequency, $\text{cm}^{-1}$	Bond Type	Literature
$\text{Al}_2\text{O}_3$	3749	linear isolated Al-OH	[30–37]
	3680	bridged OH	
	3576	H-bonded OH	
	3264	contaminants	
$\text{SiO}_2$	3742	isolated Si-OH	[25,35,36,38–42]
	3601 (shoulder)	bridged OH (or SiOH nests)	
CaMgAlO	3726	linear isolated Al-OH	[35,37,43–45]
	3767 (shoulder)	linear isolated Mg-OH	
	3677	bridged OH *	
NaSiAlO	3592	H-bonded OH	[30–37]
	3740	isolated Si-OH	[25,35,36,38–42]
3660	bridged OH		

\* Probably the bridge is formed between Ca and Al as it was reported for Ca-BEA [46].

The results for the mixed-component supports, i.e., CaMgAlO and NaSiAlO, are presented in Figure 10, Tables 2 and 3. For both these supports, the appearance of a wide band upon  $\text{CD}_3\text{CN}$  adsorption can be seen. The assignment of all the bands is given in Tables 2 and 3. The difference of the spectra before and after  $\text{CD}_3\text{CN}$  adsorption gives the values of the shifts of 236 and 195  $\text{cm}^{-1}$  for the sample CaMgAlO and 296  $\text{cm}^{-1}$  in the case of NaSiAlO. It indicates that the sample CaMgAlO contains weak BAS on the surface, while NaSiAlO contains BAS of moderate strength, which can be explained by the presence of silicon in the composition. Both these observations are proven by the shifts of the  $\text{C}\equiv\text{N}$  stretching vibration band. Both these samples demonstrate LAS on the surface, which remains in the spectra after thermal desorption up to 100 °C. BAS bands disappeared first for both samples.

**Table 3.** The shifts of stretching vibrations of CN groups upon interaction with CD<sub>3</sub>CN (strong base) and the blue shift of stretching  $\nu$  C $\equiv$ N vibrations compared to the gas phase frequency (2253 cm<sup>-1</sup>) [35,37,47,48].

Sample	Frequency, cm <sup>-1</sup>	Blue Shift of CN Stretching Vibration, cm <sup>-1</sup>	Corresponding Sites *
Al <sub>2</sub> O <sub>3</sub>	2319	66	LAS
	2262	9	bridged hydroxyl groups
SiO <sub>2</sub>	2276	23	moderate BAS
CaMgAlO	2320	67	LAS
	2259	6	bridged hydroxyl groups
NaSiAlO	2327	64	LAS
	2272	19	moderate BAS

\* BAS—Broensted acid sites. LAS—Lewis acid sites.

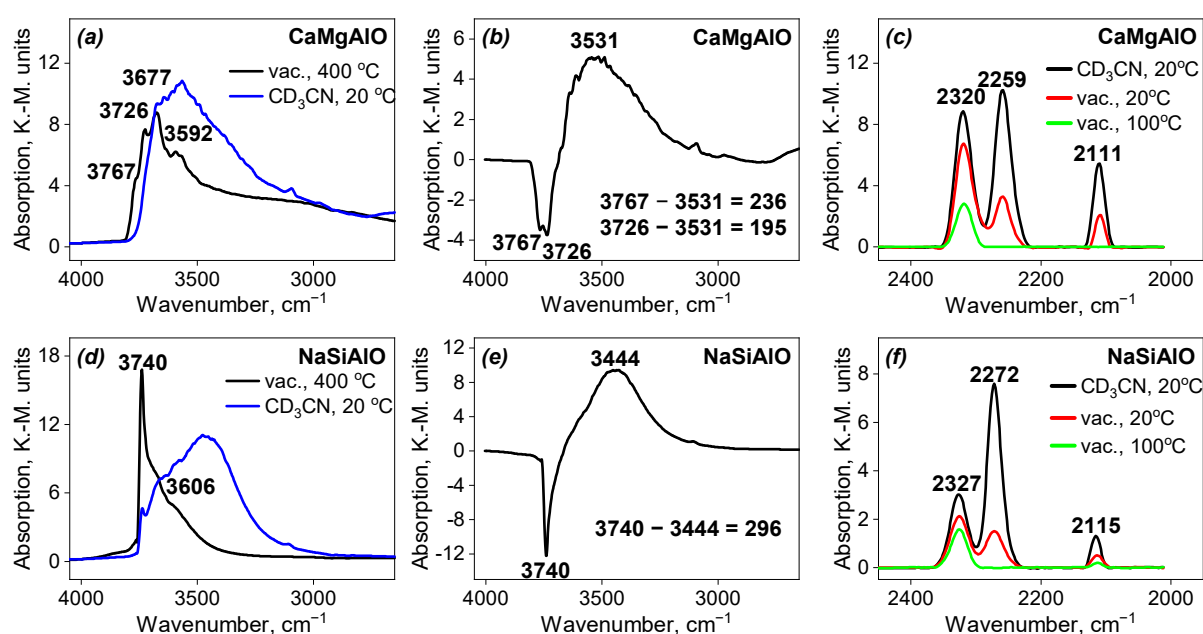


**Figure 10.** Spectra of mixed-component supports: (a,d) DRIFT-OH after evacuation and after adsorption of CD<sub>3</sub>CN; (b,e) difference of the DRIFT-OH spectra before and after adsorption of CD<sub>3</sub>CN; (c,f) DRIFT-CD<sub>3</sub>CN adsorption-desorption spectra of the support.

The strength of Broensted acid sites increases in the order: SiO<sub>2</sub>  $\cong$  NaSiAlO > CaMgAlO > Al<sub>2</sub>O<sub>3</sub> (Table 2). The strength of Lewis acid sites is about the same for all the samples, excluding SiO<sub>2</sub>, which does not demonstrate any Lewis acidity.

### 3.7. XPS

The XPS investigation was performed for all the catalysts (Table 4) and the state of rhodium on the surface was examined (Table 5). The found compositions are close to the calculated ones. The weight percentage of Rh atoms on the surface differs from the value expected by design: it might be the result of an inhomogeneous distribution of rhodium atoms assuming the local nature of the analysis. Nevertheless, the obtained values are close to the desirable 1 wt%. The error of the method let us perform only a qualitative estimation of the Rh content on the surface.

**Table 4.** The atomic concentrations of the elements on the surface of non-reduced rhodium-loaded catalysts by XPS.

Sample	O, ( $\pm 1.0$ ) at. %	Al, ( $\pm 0.3$ ) at. %	Si, ( $\pm 0.3$ ) at. %	Rh, ( $\pm 0.1$ ) at. %	Rh, wt%
SiO <sub>2</sub>	65.8	—	30.9	0.1	0.5
NaSiAlO	63.8	17.6	13.2	0.1	0.5
CaMgAlO	60.0	32.2	—	0.3	1.7
Al <sub>2</sub> O <sub>3</sub>	58.1	33.5	—	0.2	1.1

**Table 5.** TPR-H<sub>2</sub> results for non-reduced catalysts.

Sample	T <sub>max</sub> for Main Peaks, °C	H <sub>2</sub> /Rh Ratio (mol.)
1Rh/SiO <sub>2</sub>	−7, +43, +425	1.62
1Rh/Al <sub>2</sub> O <sub>3</sub>	+185, +330	1.96
1Rh/CaMgAlO	+230, +400	2.03
1Rh/NaSiAlO	−15, +390, +460	2.38

### 3.8. TPR-H<sub>2</sub>

The results of TPR-H<sub>2</sub> examinations are shown in Figure 11 and Table 5. All the rhodium-loaded samples demonstrate peaks of hydrogen consumption in the region of low temperatures. By the way, the additional peaks at higher temperatures but still below the zero line can be seen only for the silica-containing samples. It can be attributed to the interactions of rhodium (probably, oxide) particles with the support, particularly, with the silica species. Furthermore, such samples demonstrate high-temperature peaks at significantly higher temperatures than the peaks of alumina-based samples (the shift is more than 200 °C). Being compared, the silica-containing samples differ in that they have peaks of hydrogen desorption of low intensities at different temperatures: the relatively wide peak of hydrogen desorption for the sample 1Rh/SiO<sub>2</sub> is found at the temperature of 175 °C, while the sample 1Rh/NaSiAlO demonstrates two small peaks at 105 and 150 °C. At the same time, the maximal intensity peak is located at about 45 °C for the sample 1Rh/SiO<sub>2</sub>, while in the case of the sample 1Rh/NaSiAlO, it is found in the region of about 400 °C. Such a difference in reducibility may be caused by the difference in the composition of the sample: the silicon oxide species seem to provoke the reduction of rhodium oxide particles at much lower temperatures: it obviously also resulted from the smaller size of particles in the case of the SiO<sub>2</sub>-based catalyst, which can be attributed to the specific interactions between the active phase and the support. Additionally, the narrowness of the peak of hydrogen consumption at about 45 °C allowed us to propose the relative uniformity of the rhodium-oxide particles by their size.

The most low-temperature peaks are related to argon desorption. The peaks at temperatures above −60 °C can be attributed to hydrogen consumption. Additionally, we can see small peaks of hydrogen desorption only for the silica-containing samples over the region of about 200 °C. In the case of the sample 1Rh/SiO<sub>2</sub>, such a desorption peak constitutes about 1.5% of the overall hydrogen consumption, while in the case of the sample 1Rh/NaSiAlO—only 0.7%. In the case of the other samples, which do not contain any silicon, no desorption peaks can be seen at all. So, these peaks can be attributed to silicon-containing samples only.

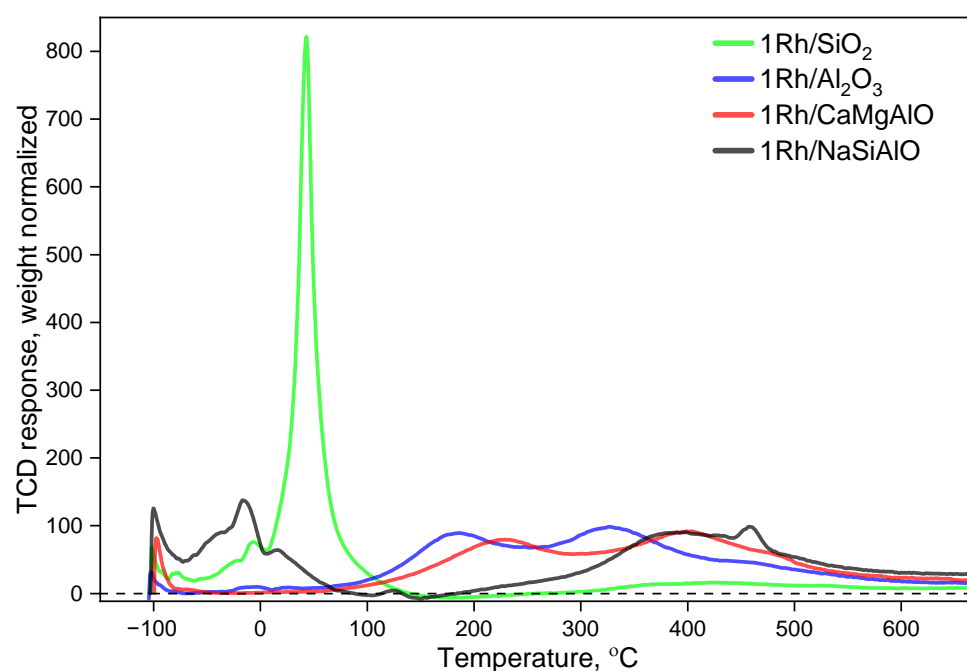


**Figure 11.** TPR-H<sub>2</sub> profiles for the rhodium-loaded catalysts.

The overall hydrogen consumption ( $H_2/Rh$ ) decreases in the following order: 1Rh/NaSiAlO > 1Rh/CaMgAlO  $\approx$  1Rh/Al<sub>2</sub>O<sub>3</sub> > 1Rh/SiO<sub>2</sub>. The hydrogen consumption at temperatures below 300 °C along with Rh reduction could also correspond to the chemical adsorption of hydrogen on the surface of the samples and the surface rehydroxylation by hydrogen activated over Rh<sup>0</sup> species (from –Si–O–Si– groups). At temperatures above 300 °C the reduction of impurities that may be present in the industrially prepared supports can be also proposed. Nevertheless, the amounts of these impurities are not too large, otherwise, they would be observed by EDX or XPS. In the case of the MgO-containing support, the additional possible way is the reduction of Rh<sub>2</sub>MgO<sub>4</sub> (reduced at 425–625 °C according to the literature data [49–52]). In the case of 1Rh/Al<sub>2</sub>O<sub>3</sub>, the two observed peaks are in accordance with the literature data [53], but the temperature range in our case is shifted to higher temperatures. It may be a result of the higher particle size of rhodia. Generally, two groups of peaks are commonly distinguished: so-called “easy-to-reduce” peaks and “difficult-to-reduce” peaks [54–57].

### 3.9. The Catalytic Tests

All the prepared catalysts were tested in a cyclohexane ring opening, the results of the examinations are presented in Figure 12. All the catalysts demonstrate non-zero activities in terms of cyclohexane conversion. The trend toward increasing conversion of cyclohexane can be seen for all the samples.

The sample 1Rh/CaMgAlO shows the maximal selectivity to n-hexane at 275 °C, but it decreases significantly when the temperature increases: at the temperatures of 300 and 325 °C, the selectivity took the minimal value among all the investigated catalysts. This sample demonstrates the maximal conversion of cyclohexane at each applied temperature. It results in the maximal space-time yield of n-hexane among the catalysts at 275 and 300 °C, but at 325 °C this catalyst is the least productive. It is noticeable that the STY of n-hexane obtained using the catalyst 1Rh/CaMgAlO is about the same as for the other most productive samples (1Rh/NaSiAlO and 1Rh/Al<sub>2</sub>O<sub>3</sub>), but the temperature in the case of the sample 1Rh/CaMgAlO is 50 °C lower. The STY of n-hexane increases with increasing temperature for all the samples, except for 1Rh/CaMgAlO: in the case of this sample, the dependence is reversed. The detailed catalytic data can be found in Supplementary Materials (Table S2).

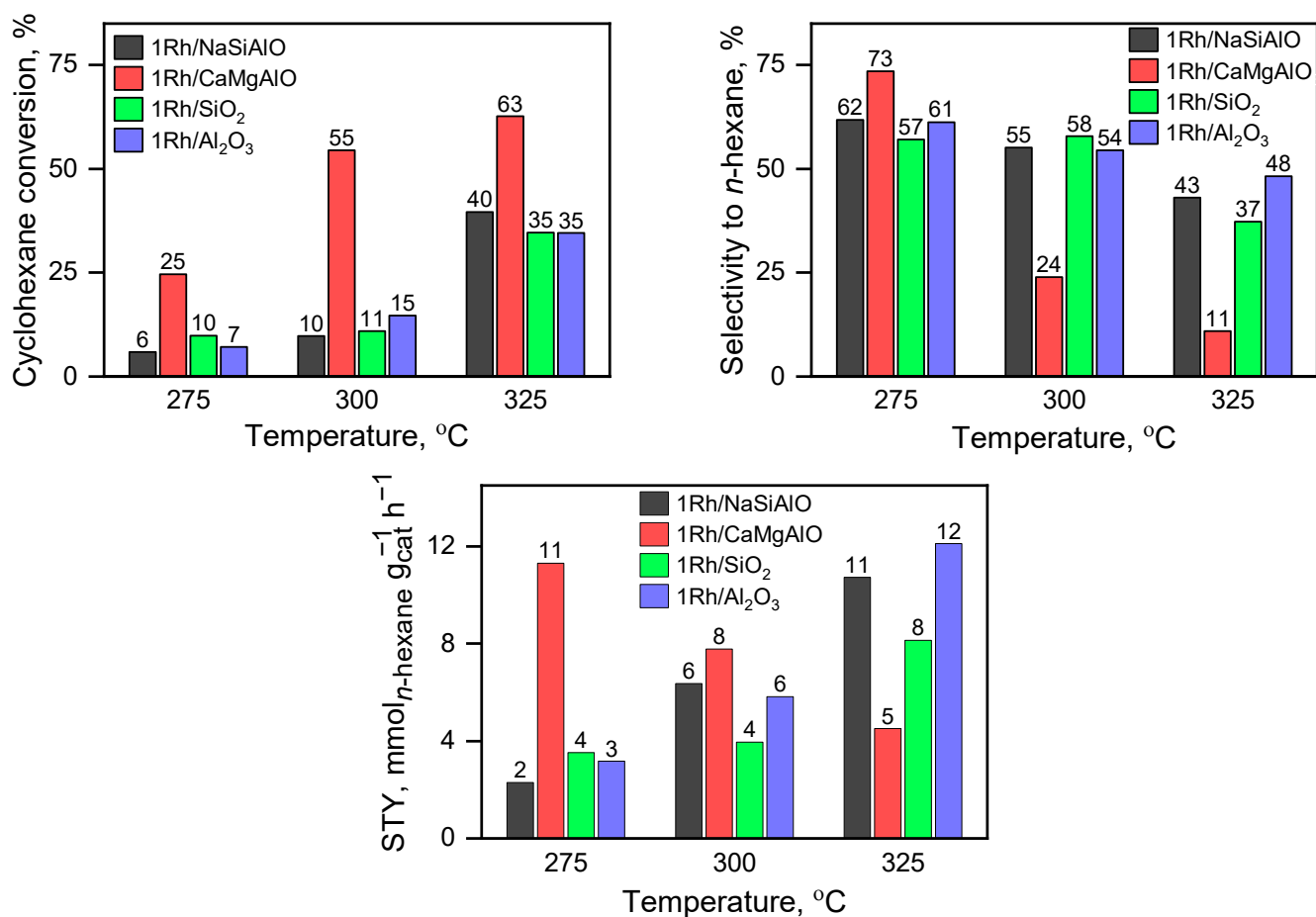


**Figure 12.** The results of the catalytic tests in cyclohexane ring opening: (left) cyclohexane conversion; (right) selectivity to *n*-hexane; (bottom) STY of *n*-hexane.

#### 4. Discussion and Conclusions

Since the samples have a similar pore size distribution, except for the sample SiO<sub>2</sub>, which has the lowest activity and selectivity to desirable products, so, the factor of the surface area and pore size distribution can be excluded from the analysis in terms of the effects on the catalytic activity and selectivity to *n*-hexane.

Phase compositions can be estimated only in terms of the intensity of the Al<sub>2</sub>O<sub>3</sub> phase reflexes, which decreases as follows: 1Rh/Al<sub>2</sub>O<sub>3</sub> > 1Rh/CaMgAlO > 1Rh/NaSiAlO. It seems to be caused by the presence of other components. The alumina phase crystallinity also should not affect the catalytic behavior dramatically. We can propose that the crystallinity of the active phase of Rh could be responsible for the difference in the catalytic activity (TPR-H<sub>2</sub> experiment), but its crystallinity cannot be estimated from the data obtained.

One can conclude from the SEM and EDX data that only the sample 1Rh/NaSiAlO demonstrates a strongly inhomogeneous rhodium distribution on the surface, and at the same time the catalytic activity of this sample is moderate, while STY of *n*-hexane is moderate too, except for the temperature of 325 °C: in this case, the STY of *n*-hexane is close to the maximal value. Possibly, agglomeration of Rh species on the surface can be the cause of the decrease in the cyclohexane conversion, while highly dispersed Rh particles favor more effective performance.

It can be seen from the data obtained by the TEM technique that the three most active samples have similar rhodia particle sizes, but SiO<sub>2</sub> has much smaller ones, then follows the sample 1Rh/NaSiAlO. Nevertheless, the conversion of cyclohexane for these samples does not differ dramatically. It is also in agreement with TPR-H<sub>2</sub> data, which revealed that the samples 1Rh/SiO<sub>2</sub> and 1Rh/Al<sub>2</sub>O<sub>3</sub> have the lowest reducibility. The distinct peak for the sample 1Rh/SiO<sub>2</sub> may also indicate the higher homogeneity of rhodium oxide particles by their size. Thus, one can see the trend in that the samples' reducibility decreases simultaneously with the decrease in the selectivity to *n*-hexane. This may be explained as follows: the species that are most active in the reaction can be produced from such reducible particles. Nevertheless, Rh nanoparticles were found in each of the reduced catalysts, but their observed amounts were different: the most abundant Rh nanoparticles were found in the samples with silica-based supports and much less—in alumina-based ones.

The results of DRIFT spectroscopy are consistent with the observations above. From the viewpoint of the catalytic activity, noticeable is the fact that the sample with the support CaMgAlO is slightly more acid in terms of BAS and the most productive to *n*-hexane at 275 and 300 °C, but not at higher temperatures because of the lower conversion of cyclohexane. This allowed us to propose that the optimal Bronsted acidity is attained in this sample. At higher temperatures, the BAS may partly disappear. It is also consistent with the literature data [31].

So, the optimal catalyst 1Rh/CaMgAlO should contain BAS with moderate strength. In this case, the attained selectivity to *n*-hexane is about 75% at the conversion of cyclohexane of 25%.

**Supplementary Materials:** The following supporting information can be downloaded at: <https://www.mdpi.com/article/10.3390/nano13050936/s1>, Additional materials on the physicochemical characterization of the samples and the catalytic data: Figure S1. TPR-H<sub>2</sub> profile of the sample 9%Rh/SiO<sub>2</sub>(Acros). Figure S2. Isotherms of N<sub>2</sub> low-temperature adsorption-desorption. Figure S3. EDX spectrum for the sample 1Rh/NaSiAlO (from TEM characterization). Figure S4. EDX spectrum for the sample 1Rh/SiO<sub>2</sub> (from TEM characterization). Figure S5. UV-visible diffuse reflectance spectra of rhodium-loaded catalysts after calcination under air atmosphere. The dashed lines demonstrate the positions of allowed transitions of supported Rh<sup>3+</sup>. Table S1. The EDX results for non-reduced catalysts: (a) 1Rh/NaSiAlO, (b) 1Rh/CaMgAlO, (c) 1Rh/SiO<sub>2</sub>, (d) 1Rh/Al<sub>2</sub>O<sub>3</sub>. Table S2. The results of catalytic tests in the cyclohexane ring opening reaction under the pressure of 40 atm. The feed mixture consisted of 0.0170 mL of cyclohexane (liquid, further vaporized) per minute and an H<sub>2</sub> (gas) flow of 50 mL per minute.

**Author Contributions:** Conceptualization, K.E.K. and A.L.K.; methodology, K.E.K., M.Y.M., E.D.F., M.Y.K., K.B.K., G.I.K., P.V.P., O.P.T., I.V.M., L.M.K. and A.L.K.; investigation, K.E.K., M.Y.M., M.Y.K., K.B.K., G.I.K., P.V.P., O.P.T., I.V.M., L.M.K. and A.L.K.; writing—original draft preparation, K.E.K. and M.Y.M.; writing—review and editing, P.V.P., L.M.K., A.L.K., G.I.K., O.P.T. and I.V.M.; visualization, K.E.K., M.Y.M., E.D.F. and M.Y.K.; supervision, A.L.K. and L.M.K.; project administration, A.L.K.; funding acquisition, A.L.K. and L.M.K. All authors have read and agreed to the published version of the manuscript.

**Funding:** The research in the part related to catalyst preparation and catalytic tests was carried out with a financial support from the grant of the Russian Science Foundation (project No. 20-73-10106). The research in the part of study of catalysts by physicochemical methods was carried out with a financial support by the Ministry of Science and Higher Education of the Russian Federation (project No. 075-15-2021-591).

**Data Availability Statement:** The data are available from the authors upon request.

**Conflicts of Interest:** The authors declare no conflict of interest. The funders had no role in the design of the study; in the collection, analyses, or interpretation of data; in the writing of the manuscript; or in the decision to publish the results.

## References

1. Moraes, R.; Thomas, K.; Thomas, S.; Van Donk, S.; Grasso, G.; Gilson, J.P.; Houalla, M. Ring Opening of Decalin and Methylcyclohexane over Alumina-Based Monofunctional  $\text{WO}_3/\text{Al}_2\text{O}_3$  and  $\text{Ir}/\text{Al}_2\text{O}_3$  Catalysts. *J. Catal.* **2012**, *286*, 62–77. [CrossRef]
2. Guan, C.; Zhai, J.; Han, D. Cetane Number Prediction for Hydrocarbons from Molecular Structural Descriptors Based on Active Subspace Methodology. *Fuel* **2019**, *249*, 1–7. [CrossRef]
3. Wei, Y.J.; Zhang, Y.J.; Zhu, X.D.; Gu, H.M.; Zhu, Z.Q.; Liu, S.H.; Sun, X.Y.; Jiang, X.L. Effects of Diesel Hydrocarbon Components on Cetane Number and Engine Combustion and Emission Characteristics. *Appl. Sci.* **2022**, *12*, 3549. [CrossRef]
4. McVicker, G.B.; Daage, M.; Touvelle, M.S.; Hudson, C.W.; Klein, D.P.; Baird, W.C.; Cook, B.R.; Chen, J.G.; Hantzer, S.; Vaughan, D.E.W.; et al. Selective Ring Opening of Naphthenic Molecules. *J. Catal.* **2002**, *210*, 137–148. [CrossRef]
5. Masloboishchikova, O.V.; Vasina, T.V.; Khelkovskaya-Sergeeva, E.G.; Kustov, L.M.; Zeuthen, P. Cyclohexane Transformations over Metal Oxide Catalysts 1. Effect of the Nature of Metal and Support on the Catalytic Activity in Cyclohexane Ring Opening. *Russ. Chem. Bull.* **2002**, *51*, 237–241. [CrossRef]
6. Vasina, T.V.; Masloboishchikova, O.V.; Khelkovskaya-Sergeeva, E.G.; Kustov, L.M.; Zeuthen, P. Cyclohexane Transformations over Metal Oxide Catalysts 2. Selective Cyclohexane Ring Opening to Form n-Hexane over Mono- and Bimetallic Rhodium Catalysts. *Russ. Chem. Bull.* **2002**, *51*, 242–245. [CrossRef]
7. Kustov, L.M.; Vasina, T.V.; Masloboishchikova, O.V.; Khelkovskaya-Sergeeva, E.G.; Zeuthen, P. Cyclohexane Ring Opening on Metal-Oxide Catalysts. *Stud. Surf. Sci. Catal.* **2000**, *130 A*, 227–232. [CrossRef]
8. Calemme, V.; Ferrari, M.; Rabl, S.; Weitkamp, J. Selective Ring Opening of Naphthenes: From Mechanistic Studies with a Model Feed to the Upgrading of a Hydrotreated Light Cycle Oil. *Fuel* **2013**, *111*, 763–770. [CrossRef]
9. Liu, Y.J.; Liang, Z.H.; Liu, X.; Yuan, L.J. Progress of Selective Ring-Opening Reaction of Decalin. *Ranliao Huaxue Xuebao/J. Fuel Chem. Technol.* **2022**, *50*, 576–582. [CrossRef]
10. Chandra Mouli, K.; Dalai, A.K. Ring Opening and Kinetics Study of Hydrotreated LGO on Ni-Mo Carbide Supported on HY and H-Beta Catalysts. *Appl. Catal. A Gen.* **2009**, *364*, 80–86. [CrossRef]
11. Blanco, E.; Piccolo, L.; Laurenti, D.; di Felice, L.; Catherin, N.; Lorentz, C.; Geantet, C.; Calemme, V. Effect of  $\text{H}_2\text{S}$  on the Mechanisms of Naphthene Ring Opening and Isomerization over  $\text{Ir}/\text{NaY}$ : A Comparative Study of Decalin, Perhydroindan and Butylcyclohexane Hydroconversions. *Appl. Catal. A Gen.* **2018**, *550*, 274–283. [CrossRef]
12. Vicerich, M.A.; Benitez, V.M.; Sánchez, M.A.; Especel, C.; Epron, F.; Pieck, C.L. Ru-Pt Catalysts Supported on  $\text{Al}_2\text{O}_3$  and  $\text{SiO}_2\text{-Al}_2\text{O}_3$  for the Selective Ring Opening of Naphthenes. *Can. J. Chem. Eng.* **2020**, *98*, 749–756. [CrossRef]
13. Vicerich, M.A.; Sánchez, M.A.; Pieck, C.L.; Benitez, V.M. Pt-Ir/ $\text{Al}_2\text{O}_3$  Catalysts for the Ring Opening of Naphthenes. Performance as a Function of Time. *React. Kinet. Mech. Catal.* **2019**, *127*, 875–886. [CrossRef]
14. D'Ippolito, S.A.; Pirault-Roy, L.; Especel, C.; Epron, F.; Pieck, C.L. Influence of Rhodium Content on the Behavior of  $\text{Rh}/\text{SiO}_2\text{-Al}_2\text{O}_3$  Catalysts for Selective Ring Opening of Decalin. *RSC Adv.* **2017**, *7*, 46803–46811. [CrossRef]
15. Govindhakannan, J.; Chandra Mouli, K.; Phoenix, A.; Fairbridge, C.F.; Dalai, A.K. Thermodynamic Equilibrium Analysis of Ring Opening of Decalin. *Fuel* **2012**, *97*, 400–410. [CrossRef]
16. Vicerich, M.A.; Benitez, V.M.; Especel, C.; Epron, F.; Pieck, C.L. Influence of Iridium Content on the Behavior of  $\text{Pt-Ir}/\text{Al}_2\text{O}_3$  and  $\text{Pt-Ir}/\text{TiO}_2$  Catalysts for Selective Ring Opening of Naphthenes. *Appl. Catal. A Gen.* **2013**, *453*, 167–174. [CrossRef]
17. Zhu, X.; Zhou, Q.; Xia, Y.; Wang, J.; Chen, H.; Xu, Q.; Liu, J.; Feng, W.; Chen, S. Preparation and Characterization of Cu-Doped  $\text{TiO}_2$  Nanomaterials with Anatase/Rutile/Brookite Triphasic Structure and Their Photocatalytic Activity. *J. Mater. Sci. Mater. Electron.* **2021**, *32*, 21511–21524. [CrossRef]
18. Zhu, X.; Wang, J.; Yang, D.; Liu, J.; He, L.; Tang, M.; Feng, W.; Wu, X. Fabrication, Characterization and High Photocatalytic Activity of Ag-ZnO Heterojunctions under UV-Visible Light. *RSC Adv.* **2021**, *11*, 27257–27266. [CrossRef] [PubMed]
19. Mouli, K.C.; Choudhary, O.; Soni, K.; Dalai, A.K. Improvement of Cetane Number of LGO by Ring Opening of Naphthenes on Pt/Al-SBA-15 Catalysts. *Catal. Today* **2012**, *198*, 69–76. [CrossRef]
20. Kustov, L.M.; Stakheev, A.Y.; Vasina, T.V.; Masloboishchikova, O.V.; Khelkovskaya-Sergeeva, E.G.; Zeuthen, P. *Dual-Function Catalysts for Ring Opening of Cyclic Compounds*; Elsevier Masson SAS: Issy Les Moulineaux, France, 2001; Volume 138. [CrossRef]
21. Kustov, L.M.; Kustov, A.L. Ring Opening of Naphthenic Hydrocarbons on Zeolite Catalysts. *Russ. J. Phys. Chem. A* **2020**, *94*, 317–322. [CrossRef]
22. Samoila, P.; Epron, F.; Marécot, P.; Especel, C. Influence of Chlorine on the Catalytic Properties of Supported Rhodium, Iridium and Platinum in Ring Opening of Naphthenes. *Appl. Catal. A Gen.* **2013**, *462–463*, 207–219. [CrossRef]
23. Piegsa, A.; Korth, W.; Demir, F.; Jess, A. Hydrogenation and Ring Opening of Aromatic and Naphthenic Hydrocarbons over Noble Metal (Ir, Pt, Rh)/ $\text{Al}_2\text{O}_3$  Catalysts. *Catal. Letters* **2012**, *142*, 531–540. [CrossRef]
24. Naranov, E.R.; Maximov, A.L. Selective Conversion of Aromatics into Cis-Isomers of Naphthenes Using Ru Catalysts Based on the Supports of Different Nature. *Catal. Today* **2019**, *329*, 94–101. [CrossRef]
25. Kustov, L.M. New Trends in IR-Spectroscopic Characterization of Acid and Basic Sites in Zeolites and Oxide Catalysts. *Top. Catal.* **1997**, *4*, 131–144. [CrossRef]
26. Thommes, M.; Kaneko, K.; Neimark, A.V.; Olivier, J.P.; Rodriguez-Reinoso, F.; Rouquerol, J.; Sing, K.S.W. Physisorption of Gases, with Special Reference to the Evaluation of Surface Area and Pore Size Distribution (IUPAC Technical Report). *Pure Appl. Chem.* **2015**, *87*, 1051–1069. [CrossRef]

27. Lin, Q.; Shimizu, K.; Satsuma, A. Kinetic Analysis of Reduction Process of Supported Rh/Al<sub>2</sub>O<sub>3</sub> Catalysts by Time Resolved in-Situ UV-Vis Spectroscopy. *Appl. Catal. A Gen.* **2012**, *419–420*, 142–147. [[CrossRef](#)]
28. Stoyanovskii, V.O.; Vedyagin, A.A.; Aleshina, G.I.; Volodin, A.M.; Noskov, A.S. Characterization of Rh/Al<sub>2</sub>O<sub>3</sub> Catalysts after Calcination at High Temperatures under Oxidizing Conditions by Luminescence Spectroscopy and Catalytic Hydrogenolysis. *Appl. Catal. B Environ.* **2009**, *90*, 141–146. [[CrossRef](#)]
29. Blasse, G.; Bril, A. Fluorescence of Rhodium-Activated Aluminum Oxide. *J. Electrochem. Soc.* **1967**, *114*, 1306. [[CrossRef](#)]
30. Tsyganenko, A.A.; Filimonov, V.N. Infrared Spectra of Surface Hydroxyl Groups and Crystalline Structure of Oxides. *Spectrosc. Lett.* **1972**, *5*, 477–487. [[CrossRef](#)]
31. Lavalley, J.C.; Bensitel, M.; Gallas, J.P.; Lamotte, J.; Busca, G.; Lorenzelli, V. FT-IR Study of the δ(OH) Mode of Surface Hydroxy Groups on Metal Oxides. *J. Mol. Struct.* **1988**, *175*, 453–458. [[CrossRef](#)]
32. Busca, G. The Surface of Transitional Aluminas: A Critical Review. *Catal. Today* **2014**, *226*, 2–13. [[CrossRef](#)]
33. Tsyganenko, A.A.; Mardilovich, P.P. Structure of Alumina Surfaces. *J. Chem. Soc. Faraday Trans.* **1996**, *92*, 4843–4852. [[CrossRef](#)]
34. Lambert, J.-F.; Che, M. The Molecular Approach to Supported Catalysts Synthesis: State of the Art and Future Challenges. *J. Mol. Catal. A Chem.* **2000**, *162*, 5–18. [[CrossRef](#)]
35. Hadjiivanov, K. Identification and Characterization of Surface Hydroxyl Groups by Infrared Spectroscopy. *Adv. Catal.* **2014**, *57*, 99–318. [[CrossRef](#)]
36. Davydov, A. *Molecular Spectroscopy of Oxide Catalyst Surfaces*; Wiley: Hoboken, NJ, USA, 2003. [[CrossRef](#)]
37. Haney, M.A.; Franklin, J.L. Mass Spectrometric Determination of the Proton Affinities of Various Molecules. *J. Phys. Chem.* **1969**, *73*, 4328–4331. [[CrossRef](#)]
38. Medin, A.S.; Borovkov, V.Y.; Kazansky, V.B.; Pelmentschikov, A.G.; Zhidomirov, G.M. On the Unusual Mechanism of Lewis Acidity Manifestation in HZSM-5 Zeolites. *Zeolites* **1990**, *10*, 668–673. [[CrossRef](#)]
39. Dessau, R. On the Presence of Internal Silanol Groups in ZSM-5 and the Annealing of These Sites by Steaming. *J. Catal.* **1987**, *104*, 484–489. [[CrossRef](#)]
40. Knözinger, H.; Huber, S. IR Spectroscopy of Small and Weakly Interacting Molecular Probes for Acidic and Basic Zeolites. *J. Chem. Soc. Faraday Trans.* **1998**, *94*, 2047–2059. [[CrossRef](#)]
41. Pelmentschikov, A.G.; van Santen, R.A.; Janchen, J.; Meijer, E. Acetonitrile-D<sub>3</sub> as a Probe of Lewis and Brønsted Acidity of Zeolites. *J. Phys. Chem.* **1993**, *97*, 11071–11074. [[CrossRef](#)]
42. Bräuer, P.; Ng, P.L.; Situmorang, O.; Hitchcock, I.; D'Agostino, C. Effect of Al Content on Number and Location of Hydroxyl Acid Species in Zeolites: A DRIFTS Quantitative Protocol without the Need for Molar Extinction Coefficients. *RSC Adv.* **2017**, *7*, 52604–52613. [[CrossRef](#)]
43. Bailly, M.; Chizallet, C.; Costentin, G.; Krafft, J.; Lauron-Pernot, H.; Che, M. A Spectroscopy and Catalysis Study of the Nature of Active Sites of MgO Catalysts: Thermodynamic Brønsted Basicity versus Reactivity of Basic Sites. *J. Catal.* **2005**, *235*, 413–422. [[CrossRef](#)]
44. Knözinger, E.; Jacob, K.-H.; Singh, S.; Hofmann, P. Hydroxyl Groups as IR Active Surface Probes on MgO Crystallites. *Surf. Sci.* **1993**, *290*, 388–402. [[CrossRef](#)]
45. Koubowetz, F.; Latzel, J.; Noller, H. Adsorption of Acetonitrile on Magnesia, an IR and TPD Study. *J. Colloid Interface Sci.* **1980**, *74*, 322–330. [[CrossRef](#)]
46. Atoguchi, T.; Kanougi, T. Phenol Oxidation over Alkaline Earth Metal Ion Exchange Beta Zeolite in the Presence of Ketone. *J. Mol. Catal. A Chem.* **2004**, *222*, 253–257. [[CrossRef](#)]
47. Angell, C.L.; Howell, M.V. Infrared Spectroscopic Investigation of Zeolites and Adsorbed Molecules. IV. Acetonitrile. *J. Phys. Chem.* **1969**, *73*, 2551–2554. [[CrossRef](#)]
48. Purcell, K.F.; Drago, R.S. Studies of the Bonding in Acetonitrile Adducts. *J. Am. Chem. Soc.* **1966**, *88*, 919–924. [[CrossRef](#)]
49. Heitnes Hofstad, K.; Hoebink, J.H.B.J.; Holmen, A.; Marin, G.B. Partial Oxidation of Methane to Synthesis Gas over Rhodium Catalysts. *Catal. Today* **1998**, *40*, 157–170. [[CrossRef](#)]
50. Ruckenstein, E.; Wang, H.Y. Temperature-Programmed Reduction and XRD Studies of the Interactions in Supported Rhodium Catalysts and Their Effect on Partial Oxidation of Methane to Synthesis Gas. *J. Catal.* **2000**, *190*, 32–38. [[CrossRef](#)]
51. Ruckenstein, E.; Wang, H.Y. Partial Oxidation of Methane to Synthesis Gas over MgO-Supported Rh Catalysts: The Effect of Precursor of MgO. *Appl. Catal. A Gen.* **2000**, *198*, 33–41. [[CrossRef](#)]
52. Tanaka, H.; Kaino, R.; Okumura, K.; Kizuka, T.; Nakagawa, Y.; Tomishige, K. Comparative Study of Rh/MgO Modified with Fe, Co or Ni for the Catalytic Partial Oxidation of Methane at Short Contact Time. Part I: Characterization of Catalysts. *Appl. Catal. A Gen.* **2010**, *378*, 175–186. [[CrossRef](#)]
53. Cuauhtémoc, I.; Del Angel, G.; Torres, G.; Angeles-Chavez, C.; Navarrete, J.; Padilla, J.M. Enhancement of Catalytic Wet Air Oxidation of Tert-Amyl Methyl Ether by the Addition of Sn and CeO<sub>2</sub> to Rh/Al<sub>2</sub>O<sub>3</sub> Catalysts. *Catal. Today* **2011**, *166*, 180–187. [[CrossRef](#)]
54. Ferrandon, M.; Krause, T. Role of the Oxide Support on the Performance of Rh Catalysts for the Autothermal Reforming of Gasoline and Gasoline Surrogates to Hydrogen. *Appl. Catal. A Gen.* **2006**, *311*, 135–145. [[CrossRef](#)]

55. Weng, W.; Pei, X.; Li, J.; Luo, C.; Liu, Y.; Lin, H.; Huang, C.; Wan, H. Effects of Calcination Temperatures on the Catalytic Performance of Rh/Al<sub>2</sub>O<sub>3</sub> for Methane Partial Oxidation to Synthesis Gas. *Catal. Today* **2006**, *117*, 53–61. [[CrossRef](#)]
56. Cimino, S.; Landi, G.; Lisi, L.; Russo, G. Rh–La(Mn,Co)O<sub>3</sub> Monolithic Catalysts for the Combustion of Methane under Fuel-Rich Conditions. *Catal. Today* **2006**, *117*, 454–461. [[CrossRef](#)]
57. Can, F.; Le Valant, A.; Bion, N.; Epron, F.; Duprez, D. New Active and Selective Rh–REO<sub>x</sub>–Al<sub>2</sub>O<sub>3</sub> Catalysts for Ethanol Steam Reforming. *J. Phys. Chem. C* **2008**, *112*, 14145–14153. [[CrossRef](#)]

**Disclaimer/Publisher’s Note:** The statements, opinions and data contained in all publications are solely those of the individual author(s) and contributor(s) and not of MDPI and/or the editor(s). MDPI and/or the editor(s) disclaim responsibility for any injury to people or property resulting from any ideas, methods, instructions or products referred to in the content.